

# Microstructure and corrosion properties of as sub-rapid solidification Mg–Zn–Y–Nd alloy in dynamic simulated body fluid for vascular stent application

Jun Wang · Ligu Wang · Shaokang Guan ·  
Shijie Zhu · Chenxing Ren · Shusen Hou

Received: 14 January 2010 / Accepted: 15 March 2010 / Published online: 30 March 2010  
© Springer Science+Business Media, LLC 2010

**Abstract** Magnesium alloy stent has been employed in animal and clinical experiment in recent years. It has been verified to be biocompatible and degradable due to corrosion after being implanted into blood vessel. Mg–Y–Gd–Nd alloy is usually used to construct an absorbable magnesium alloy stent. However, the corrosion resistant of as cast Mg–Y–Gd–Nd alloy is poor relatively and the control of corrosion rate is difficult. Aiming at the requirement of endovascular stent in clinic, a new biomedical Mg–Zn–Y–Nd alloy with low Zn and Y content (Zn/Y atom ratio 6) was designed, which exists quasicrystals to improve its corrosion resistance. Additionally, sub-rapid solidification processing was applied for preparation of corrosion-resisting Mg–Zn–Y–Nd and Mg–Y–Gd–Nd alloys. Compared with the as cast sample, the corrosion behavior of alloys in dynamic simulated body fluid (SBF) (the speed of body fluid: 16 ml/800 ml min<sup>-1</sup>) was investigated. The results show that as sub-rapid solidification Mg–Zn–Y–Nd alloy has the better corrosion resistance in dynamic SBF due to grain refinement and fine dispersion distribution of the quasicrystals and intermetallic compounds in  $\alpha$ -Mg matrix. In the as cast sample, both Mg–Zn–Y–Nd and Mg–Y–Gd–Nd alloys exhibit poor corrosion resistance. Mg–Zn–Y–Nd alloy by sub-rapid solidification processing provides excellent corrosion resistance in dynamic SBF, which open a new window for biomedical materials design, especially for vascular stent application.

## 1 Introduction

Metallic materials including stainless steel, titanium alloys, and cobalt-based alloys, due to their high strength, ductibility and good corrosion resistance, have been used as materials in vascular stent [1]. However, these metallic materials are not biodegradable in the human body and can cause long-term complication (infection and restenosis). In addition, with the passage of time, the metallic materials age gradually and are corroded in body fluids releasing of ions which have a negative impact on the body. Thus, it is necessary urgently to research the new biodegradable stents. Biodegradable stents represent an appropriate solution because of their low cost, convenience and little infection, which are favourable to patients [2]. Magnesium alloy as a degradable stent material provides both biocompatibility and suitable mechanical properties. Mg<sup>2+</sup> is present in large amount in the human body, involved in many metabolism reactions and biological mechanisms. Previous in vivo studies have shown that magnesium is suitable as degradable biomaterial for use in vascular stent [1, 3]. Compared to current polymer biodegradable stent materials, magnesium alloys have higher yield strength, which provide enough support strength. Besides, among the potential advantages of these stents, when compared to conventional stents, are the elimination of late stent thrombosis, chronic inflammation, and artifacts during noninvasive imaging.

Mg and its alloys have been previously used for biodegradable orthopedic implants [3]. However, these materials are novel in their application to coronary stents. Their mechanical and corrosion properties do not suit the requirements for stent material. AE21 [4] and WE43 [5] are two kinds of Mg-based alloys reported in the literature for making stents. But they have poor corrosion resistance and poor radial strength because of their low elastic modulus.

J. Wang · L. Wang · S. Guan (✉) · S. Zhu · C. Ren · S. Hou  
School of Materials Science and Engineering,  
Zhengzhou University, Zhengzhou 45002, Henan,  
People's Republic of China  
e-mail: skguan@zzu.edu.cn

In order to provide proper vessel wall support, the struts have to be thicker and this will increase the area of metal-artery interaction. The restenosis rate after implantation of a magnesium stent was high because rapid biocorrosion resulted in only brief opposition to vessel recoil forces.

Stable icosahedral quasicrystal phase (I-phase) with stoichiometric composition of  $Mg_{30}Zn_{60}Y_{10}$  in Mg–Zn–Y alloy system was first reported in 1993 by Luo et al. [6]. I-phase possess many interesting properties, such as high hardness, high corrosion resistance, low interface energy, etc. [7]. Recently, adding elements (Al, Mn, Ag, etc.) [8–10], heat treatment [11], ageing [12] or reworking method (hot forging, equal channel angular processed, extrusion, etc.) [13–15] by some workers to strengthen the Mg–Zn–Y alloys and improving mechanical properties of Mg–Zn–Y alloys. An approach is to prepare metal matrix composites reinforced by I-phase. Mg–Zn–Y alloys with low Zn content have a potential for biomedical application, due to its moderate strengthen, high ductility, and excellent corrosion resistance [16].

Mg–Y–Gd–Nd alloy (WE43) is usually used to construct an absorbable magnesium alloy stent. The alloying system was selected because Y and Nd are known to be beneficial in enhancing the corrosion resistance of Mg-alloys, and Mg-alloys containing Nd, Y and Gd have been shown in recent studies are not cytotoxic for implant applications [3, 17]. Besides, Zn is an essential element in the human body and it has also an even more evident strengthening effect on magnesium alloys, a magnesium alloy which contains suitable amount of Zn is a potential biodegradable alloy [18].

The aim of present study is to find a new biomedical magnesium alloy which has good corrosion properties in dynamic SBF for vascular stent application. A new biomedical Mg–Zn–Y–Nd alloy with low Zn and Y content (Zn/Y atom ratio 6) was designed, and sub-rapid solidification processing was applied to two magnesium alloys, Mg–Zn–Y–Nd and Mg–Y–Gd–Nd alloys, with and without I-phases, to evaluate the corrosion behaviour in static or dynamic SBF.

## 2 Materials and methods

### 2.1 Materials preparation

A new Mg–Zn–Y–Nd alloy was prepared by using high purity Mg, high purity Zn, Mg–25Y (wt%) (in purity 99.99 wt%) and Mg–25Nd (wt%) (in purity 99.97 wt%) master alloys by induction of mild steel crucible at approximately 740°C under  $CO_2/SF_6$  (volume fraction rate, 3000:1) atmosphere in an electronic resistance furnace. Mg–4Y–1Gd–2Nd (wt%) alloy was supplied by National Engineering Research Center of Light Alloys Net Forming [19]. The sub-

rapidly solidified bars were prepared by copper mould splat cooling method at 700°C under Ar atmosphere. The diameter of the bars was 2 mm. The cooling rate range of sub-rapid solidification is  $10^2$ – $10^3$  K/S, and the cooling rate of  $\Phi 2$  mm bars was about 200 K/s [20], which come within the cooling rate range of sub-rapid solidification.

### 2.2 Microstructure

The microstructure of the materials was characterized with scanning electron microscopy (SEM) using a field-emission electron source operating at 20.0 kV. The SEM micrograph was obtained from the etched surface using a solution of nitric acid (4 ml) and ethanol (96 ml). Constituent phases were identified by X-ray diffraction using monochromatic  $CuK_{\alpha}$  radiation. The phase compositions were analyzed by standardless energy dispersive spectrum (EDS) in scanning electron microscopy (SEM). The grain size was measured according to the linear intercept method described in the ASTM standard E112-G6.

### 2.3 Electrochemical tests

For the potentiodynamic polarisation measurements, rectangular specimens of 25 mm in length and 2 mm in width were connected to copper wire and embedded in epoxy resin with only one side exposed for the test. The exposed area was calculated by ImageTool. The working surface was ground with SiC emery papers of up to 800 grit, and finely polished with 0.5  $\mu m$  diamond powder then ultrasonically cleaned in alcohol for 5 min, then dried in air. The potentiodynamic curves were performed by means of a EG&G model potentiostat/galvanostat controlled by a computer with M352 corrosion analysis software. Experiments were performed at 37°C in a glass cell containing cycling SBF. The potentiodynamic polarisation was measured in a simulated body fluid within the normal physiological flow rate ( $2 \text{ ml}/100 \text{ ml min}^{-1}$ ) under dynamic conditions. Figure 1 shows the schematic diagram of flow

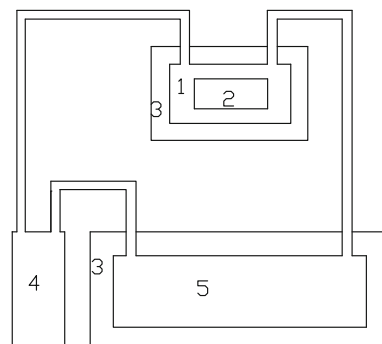


**Fig. 1** Schematic diagram of flow chamber system (1) Sample chamber; (2) Sample; (3) Water bath; (4) Pump; (5) SBF storage tank

**Table 1** Ion concentrations of SBF

Ion	K <sup>+</sup>	Na <sup>+</sup>	Ca <sup>2+</sup>	Mg <sup>2+</sup>	Cl <sup>-</sup>	HCO <sub>3</sub> <sup>-</sup>	SO <sub>4</sub> <sup>2-</sup>	HPO <sub>4</sub> <sup>2-</sup>
Concentration (mmol/L)	5.0	142.0	2.5	1.5	147.8	4.2	0.5	1.0

chamber system. The composition of SBF is listed in Table 1, which is prepared based on Ref. [21].

#### 2.4 Weight loss measurement

As cast rectangular samples for the immersion test were cut from the as cast bars directly, and were covered by epoxy resin with only one side of 1 cm<sup>2</sup> exposed for the test, while the sub-rapidly solidified bars were ground to semicircular with a rectangular plane, then other planes were covered by epoxy resin. The exposed area was calculated by ImageTool. Then the samples were immersed in SBF at 37°C for up to 7 days. The immersion solution was refreshed every 24 h. The sample weight was measured before the immersion by a balance with accuracy of 0.1 mg. After immersion, samples were cleaned in a 25 wt% chromate acid solution for about 5 min to remove the corrosion products. The specimens were then quickly washed with distilled water, dried in warm flowing air.

The dried specimens were weighed and the corrosion rate was calculated by following [22]:

$$CR = \Delta W / (At)$$

where CR is the corrosion rate, mg/cm<sup>2</sup>/h; *W* is the weight loss, mg; *A* is the original surface area exposed to the test solution, cm<sup>2</sup>, and *t* is the exposure time, hour.

### 3 Results and discussion

#### 3.1 Microstructure observation

Figure 2 shows the optical microstructures of as cast Mg–Y–Gd–Nd, Mg–Zn–Y–Nd alloys and as sub-rapid solidification Mg–Y–Gd–Nd, Mg–Zn–Y–Nd alloys. The as cast Mg–Y–Gd–Nd alloy is mainly composed of equiaxed grains and partially divorced interdendritic eutectics, marked as A in Fig. 2a. The average grain size of as-cast

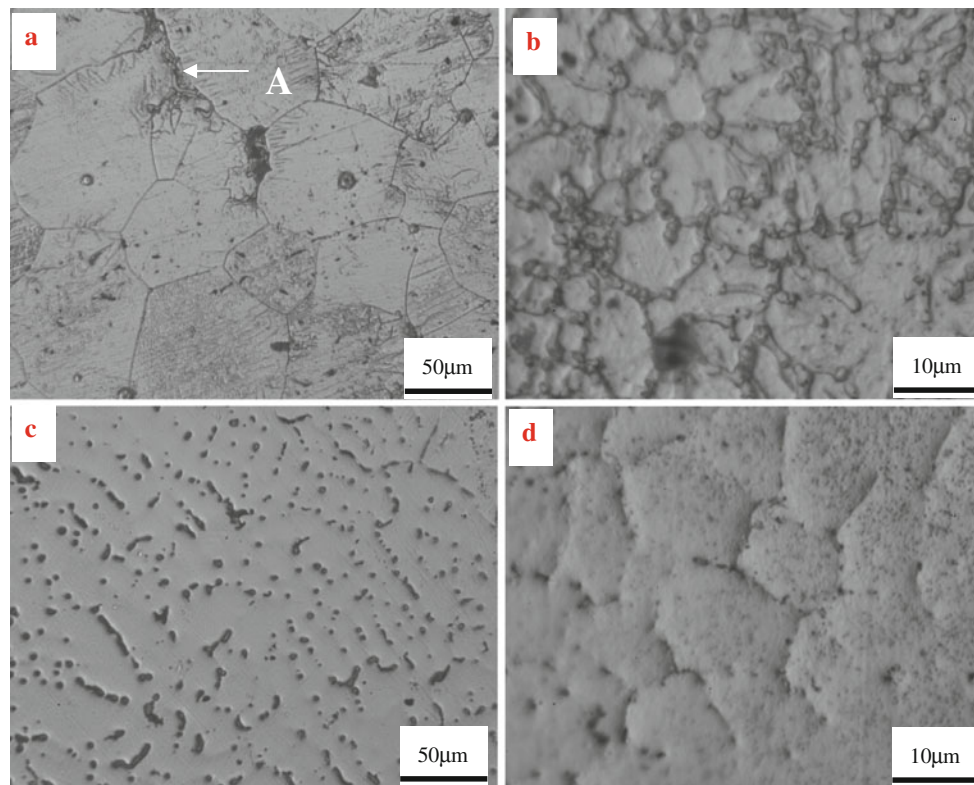


**Fig. 2** Optical image of alloys: **a** as cast Mg–Y–Gd–Nd alloy; **b** as sub-rapid solidification Mg–Y–Gd–Nd alloy; **c** as cast Mg–Zn–Y–Nd alloy; **d** as sub-rapid solidification Mg–Zn–Y–Nd alloy

Mg–Y–Gd–Nd alloy is about 70  $\mu\text{m}$ . The phase compositions of as-cast alloy by XRD analysis are shown in Fig. 3a. It demonstrates that the main intermetallic compounds in as cast Mg–Y–Gd–Nd alloy is  $\text{MgGd}_3$  phase. After sub-rapid solidification at 700°C under Ar atmosphere, from XRD result in Fig. 3b,  $\text{Mg}_2\text{Y}$  and  $\text{Mg}_{41}\text{Nd}_5$  appear. However, the microstructure of the as-cast Mg–Zn–Y–Nd alloy is different from Mg–Y–Gd–Nd alloy, which consists of two different types phases: gray phases and some small particles, shown in Fig. 2c. From XRD result, shown in Fig. 3c, the gray phases are  $\alpha\text{-Mg}$ , the particle-shaped phases are  $\text{Nd}_3\text{Zn}_{11}$  phase. These small particles distribute inside the crystal. Compared with as cast Mg–Zn–Y–Nd alloy, as sub-rapid solidification Mg–Zn–Y–Nd alloy have new phases, two new phases are identified, respectively in Fig. 3d, respond to I-phase ( $\text{Mg}_3\text{YZn}_6$ ) and  $\text{Mg}_{41}\text{Nd}_5$ . Furthermore, the average grain size of as sub-rapid solidification both Mg–Y–Gd–Nd and Mg–Zn–Y–Nd alloy is reduced significantly than the as cast ones, about 15  $\mu\text{m}$ , which is indicated clearly in Fig. 2b, d.

It is shown in the optical microstructures that the grain size of as-cast alloys are not uniform and the size of larger grains is even beyond 150  $\mu\text{m}$ . Comparison of the average grain size of samples with the same compositions under different process conditions, both Mg–Y–Gd–Nd and

Mg–Zn–Y–Nd alloys, after sub-rapid solidification, their grains refine obviously, that is, the increasing cooling rate results solute closure, grain size decrease notably and more phases appear, in the meanwhile, elements distribute more uniform.

### 3.2 Quasicrystals

A little amount of I-phase ( $\text{Mg}_3\text{YZn}_6$ , icosahedral quasicrystal structure, quasi-periodically ordered) is observed in XRD pattern (Fig. 3d). SEM microstructure of as sub-rapid solidification Mg–Zn–Y–Nd alloy (Fig. 4) reveals that the morphology of I phase is spherical.  $\text{Mg}_3\text{Zn}_6\text{Y}$  (I-phase) in Mg–Zn–Y alloys was firstly reported by Luo et al. [23]. But  $\text{Mg}_3\text{Zn}_6\text{Y}$  (I-phase) in Mg–Zn–Y–Nd alloys with low Zn low Y content (Zn/Y atom ratio 6) is firstly discovered in this study. The average grain size of quasicrystals are measured, about 500 nm.

For both Mg–Y–Gd–Nd and Mg–Zn–Y–Nd alloys, sub-rapid solidification brings different phases:  $\text{Mg}_2\text{Y}$  and  $\text{Mg}_{41}\text{Nd}_5$  appear in Mg–Y–Gd–Nd; while I-phase,  $\text{Mg}_{41}\text{Nd}_5$  are discovered in as sub-rapid solidification Mg–Zn–Y–Nd alloy. For all of the alloys, I-phase only appears in as sub-rapid solidification Mg–Zn–Y–Nd alloy, that is, the formation of I-phase is related with the solidification rate.

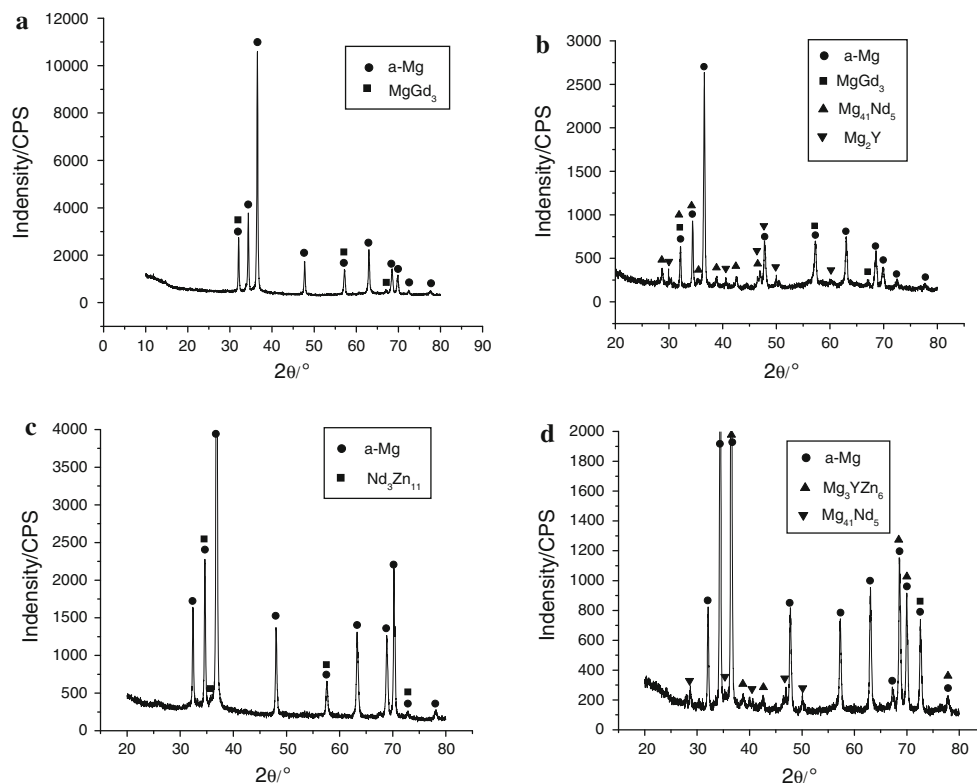
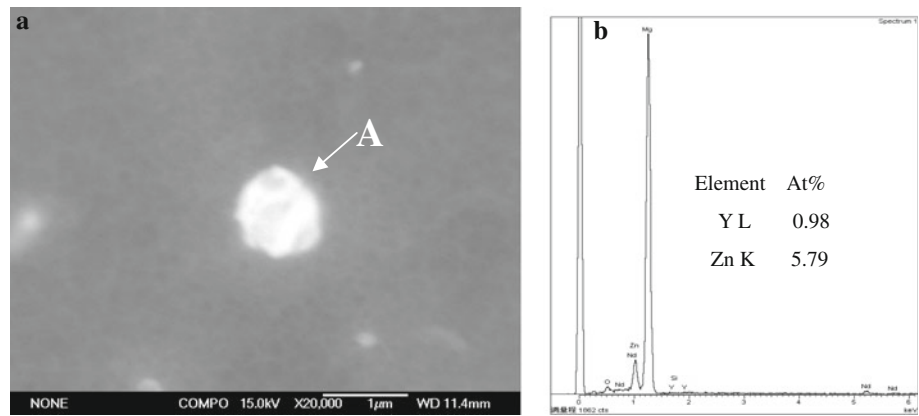


**Fig. 3** XRD patterns of alloys: **a** as cast Mg–Y–Gd–Nd alloy; **b** as sub-rapid solidification Mg–Y–Gd–Nd alloy; **c** as cast Mg–Zn–Y–Nd alloy; **d** as sub-rapid solidification Mg–Zn–Y–Nd alloy

**Fig. 4** **a** SEM morphology of spherical I-phase; **b** EDS of I phase with A in **a**



According the relation of the solidification rate and I-phase, because I-phase was metastable phase, so the solidification rate should beyond certain threshold to avoid the I-phase transform crystal; In the meantime, I-phase formed by nucleation and growing up, which were controlled by diffusion. So the sub-rapid solidification was favorable to the formation of I-phase. The growth mechanism of quasicrystal still remains an unsolved and debating problem. After the primary quasicrystal forms, it grows according its preferential crystal direction. The quasicrystal structure have two-fold, three-fold, and five-fold symmetry axes, what's more, different from the 32 kinds of classical crystal point groups, the point group of icosahedral quasicrystal exhibits  $m\bar{3}5$  [24]. The regular icosahedral quasicrystal owns twelve peak, it grow petal-like morphology if the fastest growth follows the twelve peak. However, Spherical I-phase be only discovered in this study. Because of the special nature of quasicrystals, which have the nature of both crystal and non-crystal, the alloys with I-phase will own special properties comparing with the ones without I-phase, especially its excellent corrosion-resistance property.

### 3.3 Corrosion behaviour

#### 3.3.1 The corrosion properties of different alloys in dynamic SBF

The as sub-rapid solidification alloys in this work show better corrosion properties than that of as cast ones. It indicates that the sub-rapid solidification processing can improve corrosion properties strongly. The as sub-rapid solidification Mg–Zn–Y–Nd alloy shows the highest corrosion resistance, revealing that as sub-rapid solidification Mg–Zn–Y–Nd alloy has the best corrosion properties. The corrosion potential curves in Fig. 5, polarization curves in Fig. 6 and immersion results in Figs. 7 and 8 all show the same tendency. The sub-rapid solidification processing not only brings grain refinement, but also increases solubility limit of solute atoms, expanding the scope of the alloying

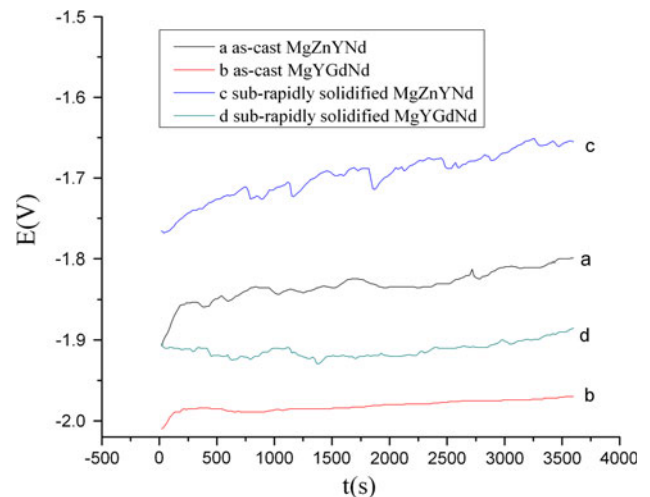


**Fig. 5** Corrosion potential curves of four alloys

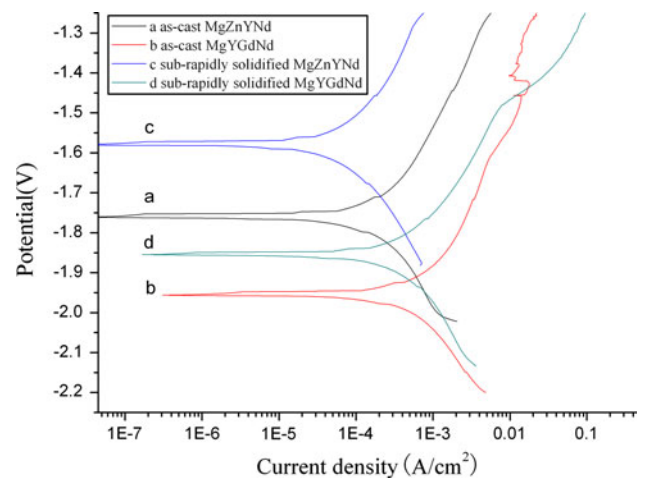


**Fig. 6** Polarization curves of alloys under different process conditions

and making the composition and microstructure more uniform, shown in Fig. 2c, d. In the meantime, the harmful impurity elements solute the a-Mg matrix, not distribute on



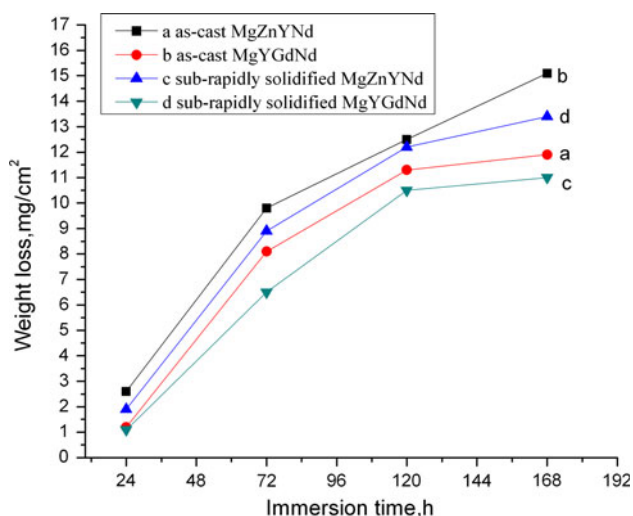


**Fig. 7** Weight loss of four alloys after immersion in SBF for up to 168 h: **a** as cast Mg–Zn–Y–Nd alloy; **b** as cast Mg–Y–Gd–Nd alloy; **c** as sub-rapid solidification Mg–Zn–Y–Nd alloy; **d** as sub-rapid solidification Mg–Y–Gd–Nd alloy

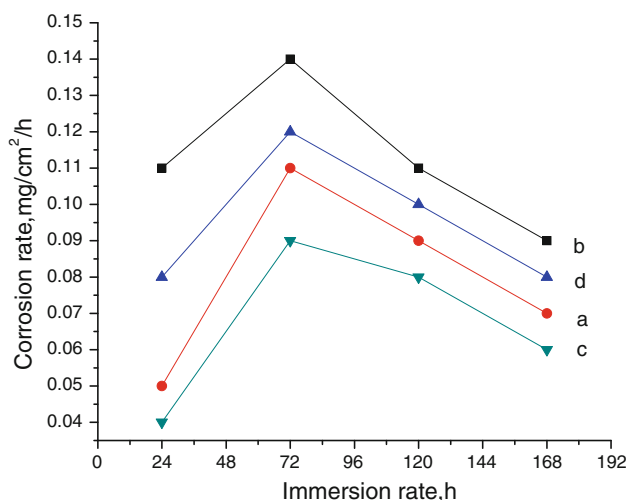


**Fig. 8** corrosion rate of four alloys after immersion in SBF for up to 168 h: **a** as cast Mg–Zn–Y–Nd alloy; **b** as cast Mg–Y–Gd–Nd alloy; **c** as sub-rapid solidification Mg–Zn–Y–Nd alloy; **d** as sub-rapid solidification Mg–Y–Gd–Nd alloy

**Table 2** Relationship of corrosion potential and corrosion current

Samples		$E_{\text{corr}}/\text{V}$	$I_{\text{corr}}/(\text{A}/\text{cm}^2)$
Mg–Y–Gd–Nd alloy	As cast	–1.95	$1.86 \times 10^{-4}$
	As sub-rapid solidification	–1.83	$1.45 \times 10^{-4}$
Mg–Zn–Y–Nd alloy	As cast	–1.76	$5.30 \times 10^{-5}$
	As sub-rapid solidification	–1.57	$2.62 \times 10^{-5}$

the grain boundary, changing the condition of grain boundary by forming self-cleaning inner surface to lessen the trend of galvanic corrosion. After sub-rapid solidification, the grain size becomes more uniform, shown in Fig. 2b, d; the stability of grain boundary increases, which can avoid the local micro-battery phenomenon. Thus, sub-rapid solidification processing can improve corrosion properties.

Corrosion potential curves and polarization curves are shown in Figs. 5 and 6. For as cast alloys, the corrosion potential (–1.95 V for Mg–Y–Gd–Nd and –1.76 V for Mg–Zn–Y–Nd) is lower than that of as sub-rapid solidification ones (–1.83 V for Mg–Y–Gd–Nd and –1.57 V for Mg–Zn–Y–Nd)(as listed in Table 2); Meanwhile, the current density of as cast or as sub-rapid solidification Mg–Zn–Y–Nd alloy has apparent reduction comparing with that of Mg–Y–Gd–Nd alloy (shown in Table 2), that is, the corrosion properties of Mg–Zn–Y–Nd alloys, as sub-rapid solidification or as cast, are better than the Mg–Y–Gd–Nd alloys. The main reasons are that: Firstly, as sub-rapid solidification Mg–Zn–Y–Nd alloys exist I-phase which is favorable to improve the corrosion properties, because it have low interfacial energy making it have stable interface; secondly, I-phase own excellent corrosion properties itself; Thirdly, it has been widely accepted that Zn can reduce the effects of Fe, Ni on corrosion properties and then improve the anticorrosion properties of Mg [25].

Figure 8 is the corrosion rate of four alloys after immersion in SBF for up to 168 h. From the corrosion rate results in Fig. 8, the corrosion rate of every alloy increases with the time increasing before 24 h, achieving the maximum at 24 h. Then, after 24 h, the corrosion rate of every alloy declines with the time increasing. This phenomenon is related with the surface of alloy in the corrosion process. Because the alloys' initial surface is smooth, the exposed area is bigger in the corrosive medium, resulting the probability of medium invasive is bigger. The invaded medium reacted with the surface of alloys. Due to the reaction exothermics, making the local temperature increased, then, the corrosion rate accelerates. With the time increasing, the corrosive conduct increased, which covered in the samples' surface, blocking the direct contact between the corrosive medium and the samples' surface, having certain protective effect. Thus, the corrosion rate of every alloy declines.

### 3.3.2 The difference of corrosion properties in dynamic and static SBF

The Mg–Zn–Y–Nd alloy in this study is designed for vascular stent application, its corrosion properties are studied in the dynamic SBF which is cycling at the same speed of body fluid, that is, the SBF in sample chamber all renew once every 50 min. we discover that, the corrosion

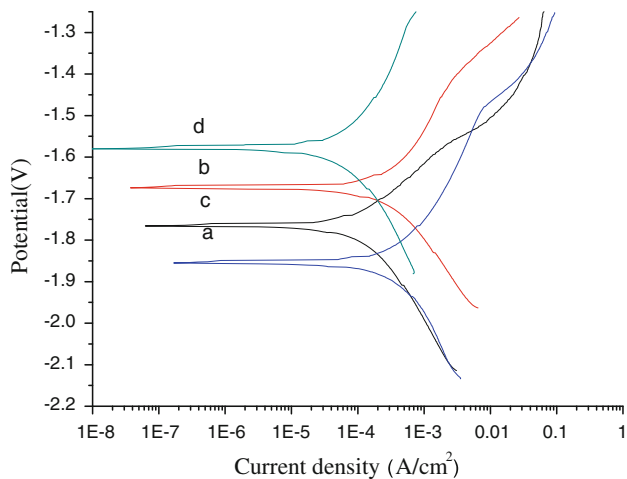
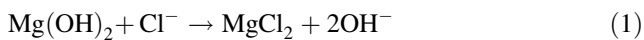


**Fig. 9** Polarization curves of as sub-rapid solidification alloys in dynamic and static SBF: **a** Mg–Y–Gd–Nd alloy in static SBF; **b** Mg–Zn–Y–Nd alloy in static SBF; **c** Mg–Y–Gd–Nd alloy in dynamic SBF; **d** Mg–Zn–Y–Nd alloy in dynamic SBF

properties of the same alloy in static SBF and dynamic SBF are different, shown in Fig. 9. For the same alloy, both Mg–Zn–Y–Nd and Mg–Y–Gd–Nd, the corrosion potential improve about 80 mv in dynamic SBF than that in static SBF, that is, dynamic SBF is favorable to the corrosion properties. In the SBF, the concentrations of  $\text{Cl}^-$  have a great influence on corrosion properties.  $\text{Cl}^-$  can lessen the corrosion properties based on the following reasons. First of all,  $\text{Cl}^-$  makes  $\text{Mg}(\text{OH})_2$  which is the sediments on samples' surface converted into  $\text{MgCl}_2$  which has higher solubility via the reaction



As a result,  $\text{Cl}^-$  increases alloys corrosion. Secondly,  $\text{Cl}^-$  has small radius to penetrate the surface film easily, leading to competitive adsorption, that is,  $\text{Cl}^-$  takes the place of  $\text{O}_2$ ,  $\text{OH}^-$  which are absorbed onto the surface of alloys to form the soluble complex. The continuously cycling dynamic SBF brings stability for  $\text{Cl}^-$  in the sample chamber, which make the corrosion morphology of alloys more uniform and the corrosion rate slower (Fig. 9). While in static SBF, as anodic reaction developing, more and more  $\text{Mg}^{2+}$  dissolve in the solution,  $\text{HCO}_3^-$  and  $\text{HPO}_4^{2-}$  are consumed, which make the concentration of  $\text{Cl}^-$  increase relatively to reduce the corrosion potential.

#### 4 Conclusions

- (1) A new biomedical alloy Mg–Zn–Y–Nd with low Zn and Y content (Zn/Y atom ratio 6) was firstly designed. The microstructure of as cast Mg–Zn–Y–Nd alloy consisted of  $\alpha\text{-Mg} + \text{Nd}_3\text{Zn}_{11}$ , while in as sub-rapid solidification Mg–Zn–Y–Nd alloy, spherical

I-phase was formed. After sub-rapid solidification, the average grain size of Mg–Y–Gd–Nd alloy and Mg–Zn–Y–Nd alloy significantly reduced, from about 700  $\mu\text{m}$  to about 15  $\mu\text{m}$ .

- (2) Sub-rapid solidification processing improves the corrosion resistance of Mg–Y–Gd–Nd and Mg–Zn–Y–Nd alloy in dynamic SBF. The corrosion potential of Mg–Zn–Y–Nd alloy rises to the maximum  $-1.57$  V after sub-rapid solidification, which is attributed to I-phases existing and grain refinement; meanwhile, the corrosion potential of as sub-rapid solidification Mg–Y–Gd–Nd alloy rises to  $-1.83$  V from  $-1.95$  V as result of grain refinement.
- (3) The corrosion potential of as cast Mg–Zn–Y–Nd alloy ( $-1.76$  V) is higher than that of as cast Mg–Y–Gd–Nd alloy ( $-1.95$  V) and as sub-rapid solidification Mg–Y–Gd–Nd alloy ( $-1.83$  V) for the reason that Zn was beneficial to improve the corrosion resistance. Simultaneously, the corrosion rate of Mg–Zn–Y–Nd alloy reduced significantly after sub-rapid solidification.
- (4) For the same alloy, either Mg–Zn–Y–Nd or Mg–Y–Gd–Nd alloy, the corrosion potential improve about more 80 mv in dynamic SBF than that in static SBF, which mainly related to the concentration of  $\text{Cl}^-$ .

**Acknowledgements** The authors are grateful for the financial supports of the National Natural Science Foundation of China (No. 30870634) and National Basic Research Program of China. (Grant NO. 2008CB617509).

#### References

1. Mani G, Feldman MD, Patel D, et al. Coronary stents: a materials perspective. *Biomaterials*. 2007;28:1689–710.
2. Zartner P, Cesnjevar R, Singer H, et al. First successful implantation of a biodegradable metal stent into the left pulmonary artery of a preterm baby. *Catheter Cardiovasc Interv*. 2005;66:590–4.
3. Staiger MP, Pietak AM, Huadmai J, et al. Magnesium and its alloys as orthopedic biomaterials: a review. *Biomaterials*. 2006;27:1728–34.
4. Heublein B, Rohde R, Kaese V, Niemeier M, et al. Biocorrosion of magnesium alloys: a new principle in cardiovascular implant technology? *Heart*. 2003;89:651–6.
5. Di Mario C, Griffiths H, Goktekin O, et al. Drug-eluting bioabsorbable magnesium stent. *Interv Cardiol*. 2004;17:391–5.
6. Luo ZP, Zhang SQ, Tang YL, et al. Quasicrystals in as-cast Mg–Zn–RE alloys. *Scripta Metall Mater*. 1993;28:1513.
7. Lee JY, Lim HK, Kim DH, et al. Effect of volume fraction of quasicrystal on the mechanical properties of quasicrystal-reinforced Mg–Zn–Y alloys. *Mater Sci Eng A*. 2007;449:987–90.
8. Kima DH, Lee JY, Lim HK, et al. Effect of Al addition on the elevated temperature deformation behavior of Mg–Zn–Y alloy. *Mater Sci Eng A*. 2008;487:481–7.
9. Zhang JS, Du HW, Liang W, et al. Effect of Mn on the formation of Mg-based spherical icosahedral quasicrystal phase. *J Alloys Compd*. 2007;427:244–50.

10. Zhu YM, Morton AJ, Nie JF, et al. Improvement in the age-hardening response of Mg–Y–Zn alloys by Ag additions. *Scripta Metall Mater.* 2008;58:525–8.
11. Liu ZH, Han EH, Liu L. High-cycle fatigue behavior of Mg–Zn–Y–Zr alloy. *Mater Sci Eng A.* 2008;483:373–5.
12. Liu XB, Chen RS, Han EH, et al. Effects of ageing treatment on microstructures and properties of Mg–Gd–Y–Zr alloys with and without Zn additions. *J Alloys Compd.* 2008;465:232–8.
13. Garce's G, Müller A, Onorbe E, et al. Effect of hot forging on the microstructure and mechanical properties of Mg–Zn–Y alloy. *J Mater Process Technol.* 2008;206:99–105.
14. Zheng MY, Xu SW, Wua K, Kamado S, et al. Superplasticity of Mg–Zn–Y alloy containing quasicrystal phase processed by equal channel angular pressing. *Mater Lett.* 2007;61:4406–8.
15. Guo XF, Shechtman D. Reciprocating extrusion of rapidly solidified Mg–6Zn–1Y–0.6Ce–0.6Zr alloy. *J Mater Process Technol.* 2007;187–188:640–4.
16. Zhang EL, He WW, Du H, et al. Microstructure, mechanical properties and corrosion properties of Mg–Zn–Y alloys with low Zn content. *Mater Sci Eng A.* 2008;488:102–11.
17. Witte F, Kaese V, Haferkamp H, et al. In vivo corrosion of four magnesium alloys and the associated bone response. *Biomaterials.* 2005;26:3557–63.
18. Song GL. Control of biodegradation of biocompatible magnesium alloys. *Corros Sci.* 2007;49:1696–701.
19. Fu PH, Peng LM, Jiang HY, et al. Fracture behavior and mechanical properties of Mg–4Y–2Nd–1Gd–0.4Zr (wt%) alloy at room temperature. *Mater Sci Eng A.* 2008;486:572–9.
20. Inoue A, Kato A, Zhang T, et al. Mg–Cu–Y amorphous alloys with high mechanical strengths produced by a metallic mold casting method. *Mater Trans A.* 1991;32:609–16.
21. Kokubo T, Takadama H. How useful is SBF in predicting in vivo bone bioactivity? *Biomaterials.* 2006;27:2907–15.
22. Liu C, Xin Y, Tang G, Chu PK. Influence of heat treatment on degradation behavior of bio-degradable die-cast AZ63 magnesium alloy in simulated body fluid. *Mater Sci Eng A.* 2007;456:350–7.
23. Luo ZP, Zhang SQ, Tang YL, et al. On the stable quasicrystals in slowly cooled Mg–Zn–Y alloys. *Scripta Metall Mater.* 1994;32:1411–6.
24. Shechtman D, Blech I, Gratias D, et al. Metallic phase with long-range orientational order and no translational symmetry. *Phys Rev Lett.* 1984;53:1951–3.
25. Boehlert CJ, Knittel K, Venkatesan K. The microstructure, tensile properties and creep behavior of Mg–Zn alloys containing 0–4.4wt% Zn. *Mater Sci Eng A.* 2006;417:315–21.